Am J Physiol Heart Circ Physiol 307: H152–H164, 2014.
First published May 9, 2014; doi:10.1152/ajpheart.00995.2013.

Cell-generated traction forces and the resulting matrix deformation modulate microvascular alignment and growth during angiogenesis

Clayton J. Underwood,[1] Lowell T. Edgar,[1] James B. Hoying,[2] and Jeffrey A. Weiss[1]

[1]*Department of Bioengineering, and Scientific Computing and Imaging Institute, University of Utah, Salt Lake City, Utah; and* [2]*Division of Cardiovascular Therapeutics, Cardiovascular Innovation Institute, University of Louisville, Louisville, Kentucky*

Submitted 18 December 2013; accepted in final form 7 May 2014

Underwood CJ, Edgar LT, Hoying JB, Weiss JA. Cell-generated traction forces and the resulting matrix deformation modulate microvascular alignment and growth during angiogenesis. *Am J Physiol Heart Circ Physiol* 307: H152–H164, 2014. First published May 9, 2014; doi:10.1152/ajpheart.00995.2013.—The details of the mechanical factors that modulate angiogenesis remain poorly understood. Previous in vitro studies of angiogenesis using microvessel fragments cultured within collagen constructs demonstrated that neovessel alignment can be induced via mechanical constraint of the boundaries (i.e., boundary conditions). The objective of this study was to investigate the role of mechanical boundary conditions in the regulation of angiogenic alignment and growth in an in vitro model of angiogenesis. Angiogenic microvessels within three-dimensional constructs were subjected to different boundary conditions, thus producing different stress and strain fields during growth. Neovessel outgrowth and orientation were quantified from confocal image data after 6 days. Vascularity and branching decreased as the amount of constraint imposed on the culture increased. In long-axis constrained hexahedral constructs, microvessels aligned parallel to the constrained axis. In contrast, constructs that were constrained along the short axis had random microvessel orientation. Finite element models were used to simulate the contraction of gels under the various boundary conditions and to predict the local strain field experienced by microvessels. Results from the experiments and simulations demonstrated that microvessels aligned perpendicular to directions of compressive strain. Alignment was due to anisotropic deformation of the matrix from cell-generated traction forces interacting with the mechanical boundary conditions. These findings demonstrate that boundary conditions and thus the effective stiffness of the matrix regulate angiogenesis. This study offers a potential explanation for the oriented vascular beds that occur in native tissues and provides the basis for improved control of tissue vascularization in both native tissues and tissue-engineered constructs.

angiogenesis; strain; orientation; morphometry; image analysis; deformation

ANGIOGENESIS, THE GROWTH OF new vessels from existing vessels, leads to the expansion of a microvascular bed. Sprouting angiogenic neovessels advance through the tissue space as they grow and extend away from the parent vessel. As angiogenic neovessels expand the vascular network to form a new vasculature, successful neovascularization requires that the topology of the new network meets the specific perfusion and functional requirements for that tissue (36). For example, alignment of both collagen fibers and blood vessels along the direction of loading is a critical step in tendon repair and healing (20). Additionally, neurons in peripheral tissues are aligned along blood vessels, and numerous molecular signals that regulate axonal guidance also affect blood vessel guidance as well, suggesting that blood vessel alignment plays a role in the establishment of functional nerve regeneration (27). Within the field of tissue engineering, repairing or replacing tissues with highly ordered vasculature requires the ability to direct neovascularization and induce alignment. However, significant gaps remain in our understanding of the mechanisms that determine the spatial organization of angiogenic growth and the topology of the resulting vascular network. Although the role of biochemical factors in angiogenic growth has been studied extensively (1, 11, 22), very few studies have directly addressed how mechanical factors influence the topology of the vascular network.

Mechanical forces affect nearly every aspect of cellular motility, metabolism, proliferation, and differentiation, and presumably the endothelial cells and pericytes that participate in the process of angiogenesis are not excluded from their effects (7, 10, 21, 23, 33, 35, 41). There is a tightly regulated balance between mechanical forces that are applied to the extracellular matrix (ECM) and their effects on endothelial cell phenotype (7, 10, 18), with the ECM mediating initial cellular mechanotransduction (13). The subsequent response of cells to mechanical stimuli is modulated by the structure and composition of the ECM (44), and the manner in which cellular structures may be connected to ECM components (19). The ECM is subsequently remodeled and reorganized by protease production, cell-matrix adhesions, and cellular force generation (23). The mechanisms by which mechanical forces and ECM structure, composition, and mechanical boundary conditions influence angiogenic sprouting and growth are poorly understood.

Previously, we investigated the mechanical regulation of angiogenesis using an in vitro model that involves culture of isolated microvessel fragments within a three-dimensional (3D) type I collagen gel, producing 3D vascularized constructs (23, 24). During culture, neovessels growing from the parent microvessel fragments interact with the collagen fibrils in the matrix, generating deformation of the surrounding fibrils. When the constructs were unconstrained at the boundaries, the constructs contracted inward homogeneously in all directions and neovessels grew into a randomly oriented vascular network. Applying either a static or dynamic mechanical strain along the long axis of hexahedral constructs during growth resulted in neovessel alignment along the direction of load. However, simply anchoring the gel along the long axis without applying an axial strain resulted in similar vascular alignment. We found that static or cyclic mechanical stretch did not enhance vascular alignment over boundary constraint alone.

Address for reprint requests and other correspondence: J. A. Weiss, Dept. of Bioengineering, Univ. of Utah, 36 S. Wasatch Drive, Rm. 3100, Salt Lake City, UT 84112 (e-mail: jeff.weiss@utah.edu).

Interestingly, aligned neovessels within constrained constructs lost their alignment upon removal of the boundary constraint (8). These results suggest that neovessel orientation during angiogenesis depends on the boundary conditions of the ECM more than the externally applied load (24).

The exact mechanical factors that control microvascular alignment during angiogenesis are unclear. When a vascularized construct is unconstrained (free to contract), all faces of the construct are stress free. When vascularized constructs are grown under these conditions, the resulting neovessels do not display preferential alignment. As mentioned, constraining the long axis of the gel causes tension to develop along the constrained axis. In this case, the alignment of the neovessels along the long axis may be due to vessels aligning with the direction of tension during growth. Such uniaxial constraint of the gel also raises the effective stiffness of the matrix along this direction. Changing the effective stiffness of the ECM can alter endothelial cell growth and morphogenesis (15, 39, 40, 45). In addition, increasing the stiffness of the gel significantly along one direction causes the gel to deform anisotropically during contraction. Neovessels could become aligned as a result of this anisotropic contraction since lateral contraction of the free edges causes them to align along the stiffest direction (i.e., the constrained axis).

The objective of this study was to determine whether a strain-based mechanism is responsible for neovessel alignment during angiogenesis and to elucidate the details of the mechanism in terms of effects on angiogenic growth and morphometry of the resulting vascular bed. We compared vascular growth and orientation between vascularized constructs subjected to several different boundary conditions during growth. Manipulating the boundary conditions of the constructs allowed us to control stress and strain fields that resulted due to cell-generated traction forces during growth and to systematically isolate the determinants of vascular alignment. These experiments were complemented with a computational analysis of stress and strain fields. Together, the results provided the necessary information to determine the means by which mechanical boundary conditions regulate microvascular alignment during angiogenesis.

MATERIALS AND METHODS

Materials. Low glucose DMEM, F12 nutrient, gentamicin (50 mg/ml), and Isolectin GS-IB_4 AlexaFluor 488 conjugate were obtained from Invitrogen (Carlsbad, CA). Transferrin, insulin, selenium, putrescine, and progesterone were obtained from Sigma-Aldrich (St. Louis, MO). Type I rat tail collagen was obtained from BD Biosciences (San Jose, CA). Recombinant human vascular endothelial growth factor (rhVEGF) was obtained from Peprotech (Rocky Hill, NJ). Clostridial collagenase was obtained from Worthington Biochemical (Lakewood, NJ). Lab-Tek chambers were obtained from Fisher Scientific (Pittsburgh, PA).

Microvessel isolation and preparation of vascularized constructs. A 3D in vitro model of angiogenesis involving neovessel sprouting from intact microvessel elements was used in this study (8, 17, 23, 24, 34). Microvessel fragments were isolated from epididymal fat pads harvested from male Sprague-Dawley rats as described previously (17). Fat pads were minced into ~1 mm^3 pieces and subjected to limited digestion with 2 mg/ml Clostridium collagenase in Dulbecco's cation free phosphate buffered saline (DCF-PBS) containing 2 mg/ml bovine serum albumin at 37°C for 8 min. The solution was immediately diluted with L-15 media containing 2% fetal bovine serum to halt digestion and then centrifuged. The pellet was washed twice and resuspended in L-15 media with 2% serum and sequentially filtered through 350 μm and 30 μm sterile nylon filters. The 30 μm filter was transferred to a sterile Petri dish and washed with L-15 media to suspend the fragments. The solution was analyzed for number of microvessels and centrifuged to obtain a pellet of microvessel fragments. While on ice, type I rat tail collagen was mixed with H_2O and concentrated DMEM to obtain a 3 mg/ml collagen and 1× DMEM solution. This solution was neutralized to ~pH 7.4 with 1 N NaOH. Microvessels were immediately resuspended in collagen at a concentration of 50,000 fragments/ml. Preliminary experiments determined that this seeding density produced maximum alignment of microvessels. The resulting mixture of microvessels and liquid collagen was poured into molds and allowed to polymerize into 3D hexahedral and cylindrical vascularized constructs, as described below.

Constrained boundary conditions. Four different boundary conditions were tested for the hexahedral constructs, each producing incrementally more constraint of the boundaries of the constructs: hexahedral unconstrained (U), long axis constrained (LAC), short axis constrained (SAC), long and short axes constrained (LSAC) (Figs. 1 and 2). This nomenclature for the hexahedral constructs was chosen to denote both the constrained directions and the aspect ratio of the construct, which combine to dictate the effective stiffness in each case. The gels were also analyzed using a Cartesian axis system with the long axis of the constructs oriented along the *x*-axis and the short axis along the *y*-axis (Figs. 1 and 2). Because the boundaries of the U constructs were unconstrained, the edges were stress free. Furthermore, the expected state of strain at the center of the construct due to cell-generated traction forces was compressive along all three directions (E_{xx}, E_{yy}, and E_{zz} less than 0), with no stress (Fig. 2, first row). Any strain along a constrained dimension constrained was small and near zero. In the LAC gels, strain along the long axis (*x*-axis, E_{xx}) was constrained, whereas the constructs were free to contract and thus produce negative strain due to cell-generated traction forces along the two transverse axes (*y*- and *z*-axes, E_{yy} and E_{zz}) (Fig. 2, second row). The SAC constructs mimicked a "strip biaxial" test, wherein strain along the short axis (*y*-axis, E_{yy}) is constrained to near-zero due to the boundary constraints imposed by the steel mesh, but strain along the *x*-axis, E_{xx} varies from negative at the edges to near-zero at the center of the construct due to the larger dimension of the gel along this direction (Fig. 2, third row). The SAC constructs were free to contract along the *z*-axis and thus develop negative strain E_{zz}. In the LSAC constructs, both the long and short axes (*x*- and *y*-axes) were constrained so that the E_{xx} and E_{yy} strains would be near zero at the center of the construct. Thus the SAC and LSAC were predicted to produce similar strain and stress fields at the center of the constructs, allowing us to determine any effects from the presence of the steel mesh in the LSAC group and/or the variation of E_{xx} strain from the free edge to the center in the SAC group.

To ensure that results for the groups above were not specific to the hexahedral geometry, we also examined cylindrical constructs. Two additional sets of boundary conditions were examined, circular unconstrained (CU) and circular constrained (CC) (Figs. 1 and 2). The CU group was analogous to the U group in that the constructs were free to contract in all directions (negative E_{xx}, E_{yy}, and E_{zz}) (Fig. 2, fifth row). The CC group was analogous to the LSAC group, in that the constructs could only contract along the *z*-axis so that the E_{xx} and E_{yy} strains would be near zero at the center of the construct.

A total of seven cultures were performed for each of the six groups, with the exception of the LSAC condition ($n = 6$). Teflon molds and stainless steel meshes were used in the culture chambers to create the construct geometries and fixed boundaries, respectively. Stainless steel meshes were formed into their final configurations using custom jigs. The boundaries of the hexahedral meshes were fixed relative to one another by mesh material that extended above the top surface of the construct, above the culture media. The CC mesh consisted of a rectangular piece of mesh that was bent into a circle and then secured

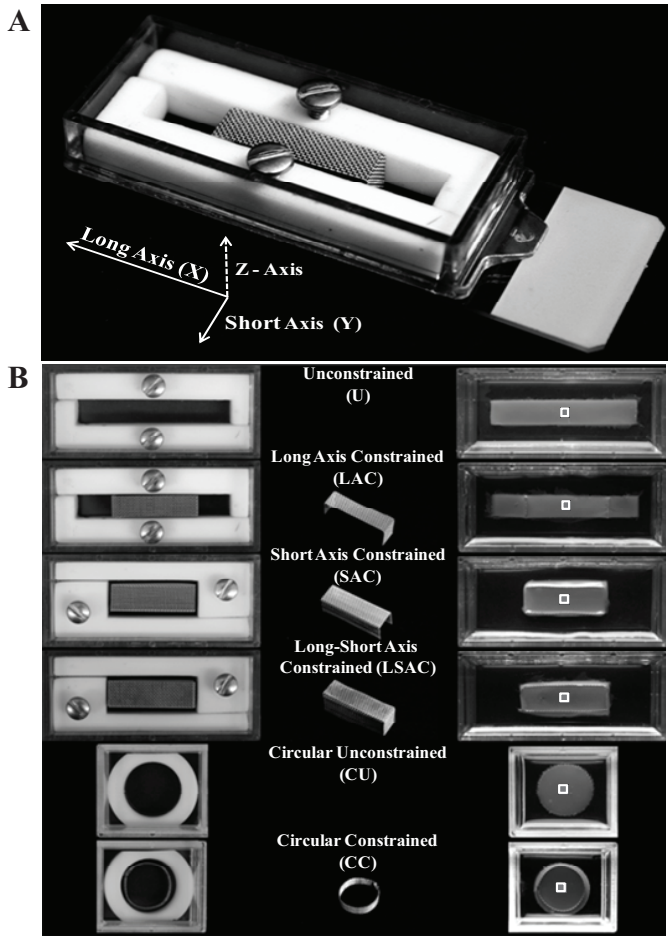

Fig. 1. Culture geometry and boundary conditions used in experiments. *A*: Lab-Tek II culture chamber containing Teflon molds and long-axis constrained (LAC) stainless steel mesh. *B*: assembled culture chambers for all boundary conditions (*left*), stainless steel meshes (*middle*), and 3-dimensional (3D) collagen cultures after removal of Teflon molds (*right*). The region that was imaged and quantified by laser scanning confocal microscopy is shown as a white box. The Lab-Tek chambers used for the hexahedral constructs measured 49 × 19 × 11 mm, whereas the chambers used in the circular constructs measured 23 × 19 × 11 mm.

to itself using the medical grade UV curable adhesive Loctite 3311 (Henkel, Rocky Mountain, CT). Hexahedral constructs were formed by pouring 0.8 ml of collagen/microvessel solution into the mold and were maintained in single-well Lab-Tek II chamber slides. One set of molds (38.5 × 6.5 × 3.0 mm) was used to create the U and LAC cultures, and another set (22.5 × 9.5 × 3.0 mm) was used for the SAC and LSAC gels. The wider molds were used in the SAC and LSAC cases to facilitate the constraint of the short axis. Cylindrical constructs were polymerized from 0.5 ml of collagen/microvessel solution in 14.5 mm diameter molds and were maintained in 2-well Lab-Tek II chambered coverglass. Cultures were allowed to polymerize for 30 min at 37°C. The Teflon molds were then removed and 3.0 or 2.0 ml of serum-free culture media was added for the hexahedral and cylindrical cultures, respectively. Serum-free culture media consisted of equal parts of low glucose DMEM and F21 nutrient, which was supplemented with insulin, transferrin, and selenium (6, 24). Media was changed after 2 and 4 days in culture.

Measurement of gel contraction. Photographic images of the top and side of the contracted vascularized constructs were obtained after 6 days of culture. Gel dimensions were measured from the images using ImageJ (37). The scale for each image was calibrated using a fiducial placed at the same focal depth for each culture. Dimensions of acellular gels were used as the reference (*day 0*) dimensions of the vascularized constructs. Measurements at *day 6* were taken at the center of the construct, away from any boundary constraints. Engineering strain was calculated by taking the difference in dimensions between *day 6* and *day 0*, and then normalizing by the reference length at *day 0*. For cylindrical constructs, diameter was measured to calculate the degree of contraction. Length measurements for the LSAC and CC groups could not be obtained along the unconstrained dimension due to optical obstruction by the wire mesh. Volumetric contraction was calculated by normalizing the change in volume by the reference volume.

Microvessel alignment and growth quantification. We examined microvessel growth and alignment at the center of each construct using 3D mosaic image datasets obtained by laser scanning confocal microscopy. After 6 days of growth, the cultures were fixed in a 1× PBS solution containing 4% paraformaldehyde for 24 h. Cultures were washed with 1× PBS containing 0.1% Triton X-100, and endothelial cells were stained overnight with 1 μg/ml Isolectin GS-IB_4 conjugated to Alexa 488 (Invitrogen). Cultures were washed with the same buffer without isolectin conjugate before imaging. Datasets (3D image) of endothelial cells were obtained via laser scanning confocal microscopy. Each dataset consisted of four adjacent 10× stacks of 121 images with a 2.5 μm step size, covering a depth of 300 μm. Hexahedral constructs were oriented with the long axis parallel to the horizontal imaging axis (*x*-axis). Imaging was performed at the center region of each culture. Other select areas near the constrained or free boundaries were also imaged. The datasets were median filtered, deconvolved, and skeletonized to obtain the 3D morphometry of the microvessels using the AMIRA software (Visage Imaging, San Diego, CA) as described previously (24).

Measurement of growth and alignment were obtained from the skeletonized data using WinFiber3D, a custom software package that can be used to quantify morphometric statistics in 3D line segment networks (30). The angles of each skeletonized line segment relative to the *x*- and *z*-axes of the cultures were determined. Length-weighted distributions of orientation angles were computed. Because the cylindrical gels did not have an axis for reference, the fast Fourier transform (FFT) was used to characterize orientation in their image data. FFT analysis was performed on the Z-projections of each of the four adjacent data stacks in MATLAB (MathWorks, Natick, MA) as described previously (2). Polar plots of the angular frequency of vessel orientation were generated as well as the magnitude of orientation (anisotropy). An anisotropy value of 0.0 represents a random orientation, whereas a value of 1.0 represents complete alignment of vessels. FFT analysis of phantom images was used to test the validity of this method.

WinFiber3D was used to compute vascularity, average segment length, and total number of vessel branch points. Vascularity was defined as the sum total of the length of all microvessels divided by the volume of the imaged region. Average segment length was calculated from the length of line segments, which included the distance between branch points and the distance from branch points to end points. The total number of branch points was normalized by the total length of vessels in the culture.

Assessment of elastic stress in long-axis constrained constructs. To determine whether LAC vascularized constructs were under elastic stress due to cell-induced compaction, cutting experiments were performed. LAC constructs were cultured for 4 days in vitro. After 4 days, LAC gels in the control group were given fresh media, whereas LAC gels in the Cytochalasin D (CytoD) group received fresh media plus 10 μM CytoD. CytoD inhibits actin polymerization. Twenty minutes later, one end of the LAC constructs was cut free from the boundary constraint using a scalpel. Constructs were returned to the incubator, and digital images were captured 5 min later. Imaging continued every 20 min (72 images over 24 h). A glass mirror under the constructs was used to obtain multiple culture dimensions. Culture

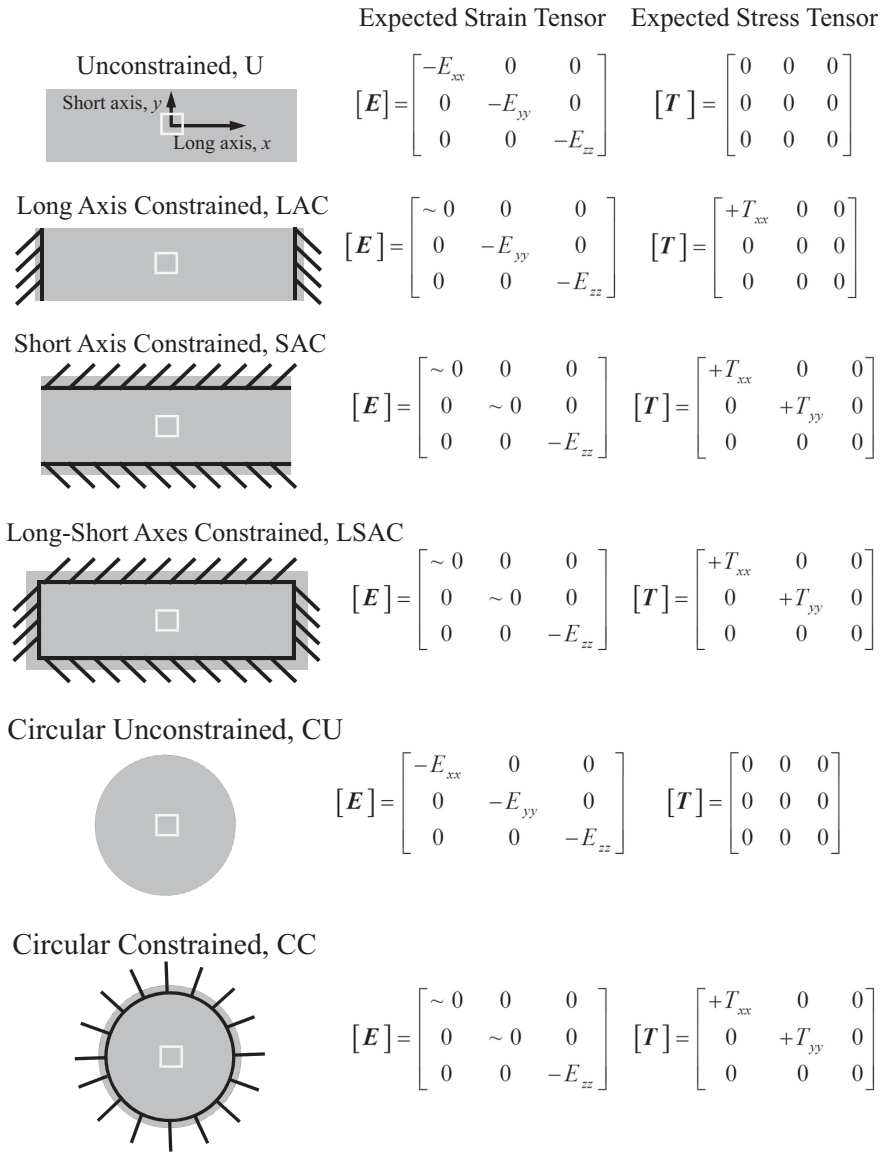

Fig. 2. Schematic showing boundary conditions for each of the 6 groups (*left*), expected state of strain [*E*] at center of construct due to cell generated traction forces (*middle*), and expected state of stress [*T*] at center of construct due to cell generated traction forces (*right*) in Cartesian coordinates. The approximate location of 3D image acquisition by laser scanning confocal microscopy is shown as a small white box. The signs (+ or −) are indicated for the expected strains and stresses, with negative signs on the strain indicating compression and positive signs on the stresses indicating tensile force. The notation "∼0" indicates that the strain component is expected to be very small relative to the others, but not necessarily exactly 0.

length, height, and width were measured with ImageJ calibrated to optical markers in the same focal plane.

Finite element analysis. To illustrate that the combined effects of cell-generated traction forces, boundary conditions, and aspect ratio could produce the measured global changes in shape of the constructs, independent of other factors, a simplified finite element (FE) model was constructed and analyzed. We analyzed the deformation of the vascularized constructs in each boundary condition case due to the effects of gel contraction via cellular traction forces. FE models of the constructs were created using PreView (30). A rectilinear domain was filled with hexahedral finite elements. A mesh convergence study demonstrated that a mesh with uniform nodal spacing of 0.5 mm produced converged predictions of global and local strain. The stainless steel mesh was represented with rigid body elements. To simulate the LAC boundary condition, rigid body elements were placed along the faces normal to the long axis (*x*-axis). To simulate the SAC boundary condition, rigid body elements were placed along the faces normal to the short axis (*y*-axis). A simple neo-Hookean hyperelastic constitutive model was used to represent the homogenized, passive, equilibrium material behavior of the culture, including the collagen fibrils, nonfibrillar matrix, and neovessels (Young's modulus E = 40.8 KPa, Poisson's ratio ν = 0.0) (8, 16). The modulus was chosen based on our previously published experimental data for uniaxial tensile testing of collagen gels (25). The Poisson's ratio was assigned a value of zero based on experimental measurements (43). A Poisson's ratio of zero is a reasonable and common choice for the equilibrium behavior of highly hydrated, highly permeable collagen gels under small strains, since the gels undergo a significant volume change during applied external stress or cellular compaction as the pore structures are collapsed and water is forced out of the material. The passive stress in the material due to deformation was calculated as $\boldsymbol{\sigma}^P = \mathrm{E}/2J\,(\boldsymbol{b} - \boldsymbol{I})$, where $\boldsymbol{\sigma}^P$ is the Cauchy stress tensor, $\boldsymbol{b}$ is the left Cauchy-Green deformation tensor, J is the Jacobian of the deformation gradient, and $\boldsymbol{I}$ is the second-order identity tensor. A model of active contractile forces based on uniform, isotropic local contraction was used to simulate the contraction of the culture by the growing microvessel fragments. The total Cauchy stress was the sum of the passive stress component $\boldsymbol{\sigma}^P$ and an active stress $\boldsymbol{\sigma}^A$ arising from cellular traction forces generated as the microvessels pull on the collagen fibers within the gel (4): $\boldsymbol{\sigma} = \boldsymbol{\sigma}^P + \boldsymbol{\sigma}^A = [\mathrm{E}/2J\,(\boldsymbol{b} - \boldsymbol{I})] - p\boldsymbol{I}$, where the magnitude of the active stress, p, represented an isotropic contractile force that was homogeneous.

Nonlinear FE simulations were performed using FEBio (www.febio.org) (31). To enable an incremental-iterative nonlinear solution

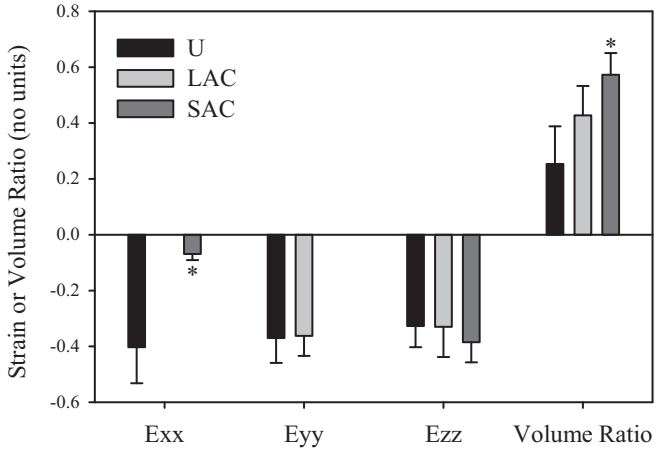

Fig. 3. Engineering strain in each direction (E_{xx}, E_{yy}, E_{zz}) and volume ratios calculated by measuring edge displacement of contracting cultures at *day 6*. No edge displacement and therefore strain occurred along the constrained directions for certain boundary conditions [$E_{xx} = 0.0$ for LAC; $E_{yy} = 0.0$ for short-axis constrained (SAC)]. The SAC group contracted only 6.9% along the *x*-axis, which was significantly less than the 40.3% for the unconstrained (U) group (*$P < 0.001$). Overall, the volume of unconstrained constructs was reduced by ~70%, whereas the volume contraction at the geometric center of the LAC constructs was 57.3% (*$P = 0.086$). The estimated volume contraction of the SAC constructs of 42.8% was significantly less than that of the unconstrained constructs (*$P = 0.001$). Bars indicate standard error.

strategy, the magnitude of the active stress p was discretized over quasi-time (32). The simulations were terminated when deformed dimensions of the mesh matched the edge displacement data of the U group at *day 6*, corresponding to an active stress magnitude of $p = 1.0$ KPa. This same value of active stress was used in the simulations of the other three boundary conditions (LAC, SAC, and LSAC). Results from the FE simulations were analyzed using PostView (29). Strain was obtained from the FE models in two ways: calculating engineering strain using edge displacements (global strain) and extracting the principal components of the infinitesimal strain tensor at the center of the construct (local strain). Strain values and changes in volume were compared with measurements of experimental constructs.

Statistical analysis. For angle distribution data, one-way ANOVAs were used to determine whether there were differences between hexahedral groups in each 10° angle bin. When significance was found, Tukey or Dunn's method post hoc tests were performed. For all other data, ANOVA was used to identify significance among the hexahedral cultures, and *t*-tests were used determine significance between circular boundary conditions.

RESULTS

The parent microvessel fragments showed minimal growth and sprouting during the first two days in culture. Sprouting neovessels were evident by *day 3*, with substantial growth occurring between *days 4* and *6*. After *day 6*, all of the constructs had contracted, demonstrated by negative strains measured along free axes and a volume ratio less than 1.0 (Fig. 3). Contraction along the long (*x*-) and short (*y*-) axes for the U group was ~40%, whereas the contraction along the *z*-axis was slightly less. Contraction in the LAC group along the *y*-axis and *z*-axis was similar to measurements from the U group. The SAC group contracted only 6.9% along the *x*-axis, which was significantly less than the 40.3% for the U group ($P < 0.001$). Overall, the volume of unconstrained constructs was reduced by ~70%, whereas the volume contraction at the geometric center of the LAC constructs was 57.3% ($P = 0.086$). The estimated volume contraction of the SAC constructs of 42.8% was significantly less than the unconstrained constructs ($P = 0.001$).

Z-projections of the 3D confocal image data revealed qualitative differences in neovessel alignment within the XY-plane between the different groups (Fig. 4). For the hexahedral constructs (Fig. 4*A*), neovessel networks in the U and LAC groups were more dense and exhibited a higher level of network complexity than the SAC and LSAC groups. Neovessels in the LAC group were oriented along the long axis of the construct, whereas neovessels in the other groups were randomly oriented. In the cylindrical constructs (Fig. 4*B*), neovessels networks in the CU group exhibited a higher density in comparison with the CC group. Neovessels in both the CU and CC groups exhibited a random orientation at the center of the constructs.

Skeletonization of the 3D confocal image datasets allowed quantification of the morphometry of the microvessel networks (Fig. 5). With the exception of the LAC group in the hexahedral constructs, there was a trend of decreasing vascularity going from the most unconstrained (U) to the most constrained (LSAC) boundary conditions (Fig. 5*A*). The LSAC group had significantly less growth than the LAC group ($P = 0.004$) and

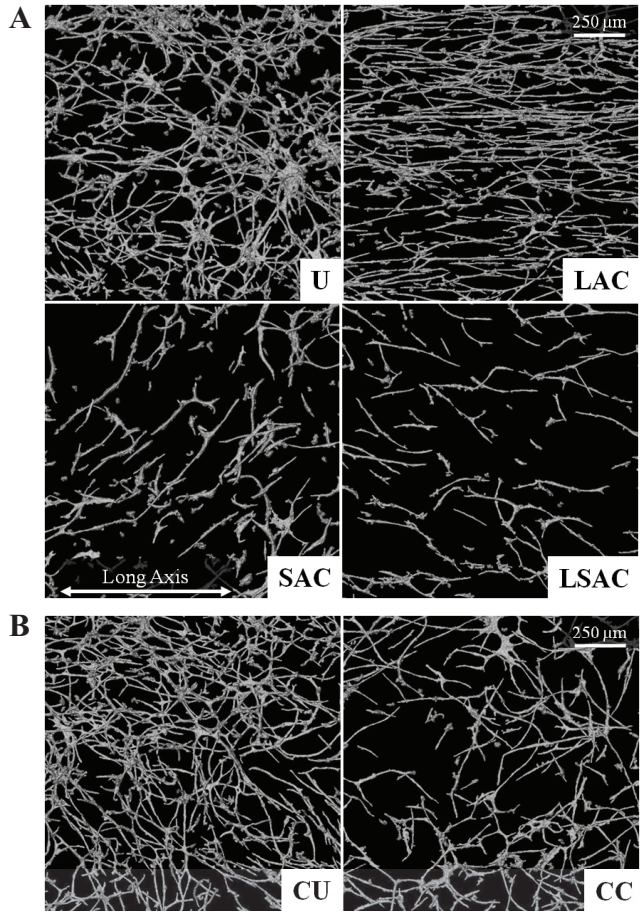

Fig. 4. Z-projections from confocal images of microvessels after *day 6*. *A*: hexahedral boundary conditions U, LAC, and SAC. During imaging, the long axis of hexahedral constructs was aligned with the horizontal (*x*-) axis of the imaging plane. *B*: circular boundary conditions, circular unconstrained (CU) and circular constrained (CC).

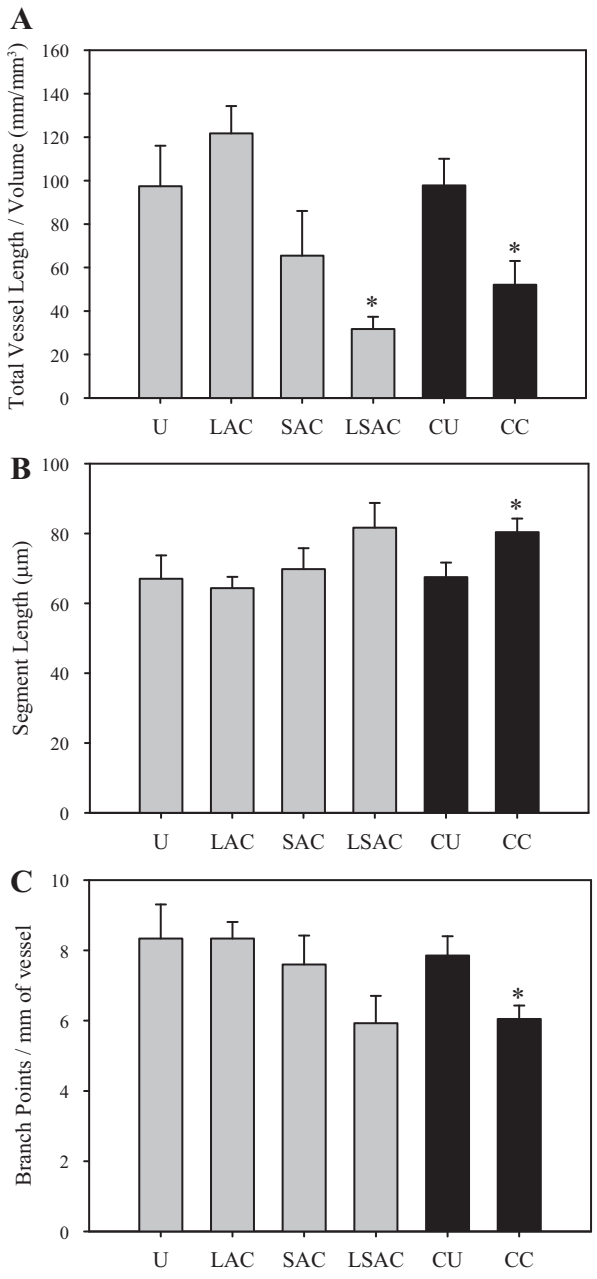

Fig. 5. Quantitative measurements of microvessel growth for different boundary conditions. *A*: microvessel vascularity tended to decrease as gels became more constrained. Vascularity for the long-short axis constrained (LSAC) group was significantly lower than that in the U ($*P = 0.004$) and LAC groups ($*P = 0.044$). Vascularity in the CC boundary condition was significantly less than that in the CU condition ($*P = 0.017$). *B*: average segment length tended to increase as the gel became more constrained. Segment length in the CC cultures was significantly greater than that in the CU cultures ($*P = 0.043$). *C*: microvessel branching tended to decrease as the gel became more constrained. Branching within the CC boundary condition culture was significantly reduced relative to the unconstrained control, CU ($*P = 0.020$). Bars indicate standard error.

the U group ($P = 0.044$). The vascularity in the CC group was also significantly reduced ($P = 0.017$) when compared with the CU group. In contrast, there was an increasing trend in segment length, which is the distance between vessel branch points, going from less constrained to more constrained groups (Fig. 5*B*). The circular constrained group had a significantly greater segment length than the circular unconstrained group ($P = 0.043$). There was decreased microvessel branching going from unconstrained to more constrained boundary conditions (Fig. 5*C*). The CC cultures had significantly less branches per unit length than the CU cultures ($P = 0.020$). There were no significant differences between the U and CU groups or between the LSAC and CC groups for any of the growth parameters.

Analysis of the angles between neovessel orientation and the long axis from the skeletonized datasets allowed for the comparison of microvessel segment orientation across boundary conditions in hexahedral constructs. In this analysis, segments exhibiting smaller angles were parallel to the long (*x*-) axis, and segments showing larger angles were parallel to the short (*y*-) axis of the hexahedral constructs. The U, SAC, and LSAC groups exhibited near-random angle distributions relative to the long axis of the cultures (Fig. 6*A*). The LAC group had a nonrandom distribution relative to the long axis of the culture, with 30% of segments in the 10° angle bin. There were progressively fewer segments in consecutive angle bins with less than 5% of segments in the 90° angle bin. Significant differences were detected between LAC and the other boundary conditions in all angle bins except for the 30° and 40° bins. Because cylindrical cultures had no long axis or other frame of reference, FFT analysis was used to quantify neovessel orientation (Fig. 6*B*). Both circular boundary conditions, as well as the U, SAC, and LSAC groups, had anisotropy indices less than 0.3. Low anisotropy values indicate a random orientation of neovessels, with a value of 0 being completely random and a value of 1 representing complete alignment. In agreement with the angle-bin distribution data, the LAC group had a high anisotropy value of 0.7, which was significantly greater than all other conditions when analyzed by FFT ($P < 0.001$). Taken together, these data indicate that neovessel orientation was random for all groups except the LAC group.

Neovessel orientation was also examined relative to the *z*-axis (direction of depth through the cultures). In this case, angle bin distributions were obtained from the skeletonized datasets for both hexahedral and cylindrical constructs (Fig. 7). For both the hexahedral and cylindrical constructs, neovessels were preferentially oriented within the XY-plane (Fig. 7, *A* and *B*). In all cases, greater than 35.0% of length-weighted segments were found in the 90° angle bin. Distributions for the LAC, SAC, and LSAC groups were nearly identical, but the distribution for the U group was slightly more random relative to the *z*-axis. Significant differences were detected between U and the other groups in the 70°, 80°, and 90° angle bins ($P < 0.01$). For the cylindrical cultures, the CU boundary cultures were more random than the CC cultures relative to the *z*-axis. Significant differences were detected in the 30°-90° angle bins ($P < 0.05$ for all cases). These results demonstrate that neovessel growth was more aligned in the horizontal plane for cultures with constrained boundaries than for cultures with unconstrained boundaries.

Neither the control nor the CytoD-treated constructs exhibited any significant contraction at 5 min after being cut away from the mesh boundary constraint (Fig. 8). Over the subsequent 24 h, control LAC gels contracted 40% along the long axis. In contrast, the CytoD-treated LAC gels did not exhibit any measureable contraction. These results verify that little if

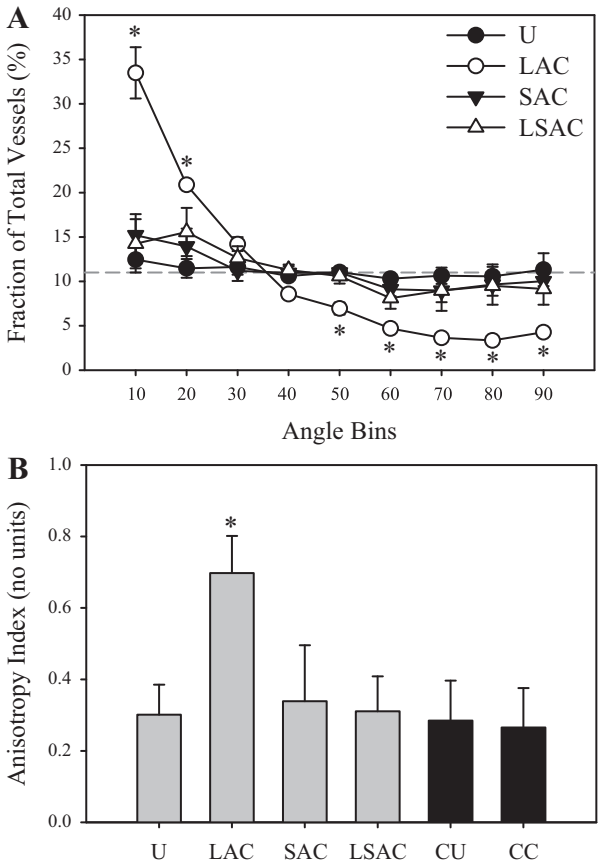

Fig. 6. Microvessel alignment and anisotropy within the XY-plane. *A*: length-normalized distributions of orientation for hexahedral constructs. The 10° bin represents angles from 0° to 10°, which are parallel to the long axis (*x*-axis). The 90° bin represents angles from 80° to 90° and is parallel to the short axis (*y*-axis). The LAC group was significantly different from at least 1 other boundary condition in all but the 30° and 40° angle bins (*$P < 0.05$). A completely random distribution should have ~11% in each angle bin, represented by the dashed line. *B*: microvessel anisotropy as determined by fast Fourier transform (FFT) analysis. A value of 0.0 represents random organization, whereas a value of 1.0 represents complete alignment. The LAC boundary condition had a significantly higher anisotropy value than all the other boundary conditions, as expected based on the angle distributions in *A*. The cylindrical constructs had similar anisotropy values to the other randomly organized hexahedral boundary conditions. The LAC group had a high anisotropy value of 0.7, which was significantly greater than all other conditions when analyzed by FFT (*$P < 0.001$). Bars indicate standard error.

any elastic stress accumulates within the ECM of LAC gels during the culture period. Furthermore, contraction after separation from the boundary constraint is due to cell-generated traction forces, which are abolished via CytoD treatment. Vascularized constructs treated with CytoD at *day 0* did not exhibit any growth or gel contraction (data not shown).

Finite element (FE) computer models were constructed to estimate the strain field throughout the vascularized gels for each of the various boundary conditions. Global engineering strain was calculated using edge displacements as the ratio of the change in length over the initial length. FE simulation of the LAC condition predicted compressive strains E_{yy} and E_{zz} (−41.0%) at the center of the sample, with small positive strain E_{xx} (3.0%) (Fig. 9*A*, *left*, and *B–D*). E_{xx}, E_{yy}, and E_{zz} were inhomogeneous along the *x*-axis due to the displacement constraint imposed by rigid-body elements modeling the wire mesh. For the SAC model (Fig. 9*A*, *right*, and *B–D*), E_{xx} and E_{yy} strains were relatively small at the geometric center (−1.0% and −12.0%, respectively), whereas E_{zz} was similar to that predicted by the LAC model (−41.0%).

In general, the FE simulations produced strains and volume ratios that were in very good agreement with experimental measurements (Fig. 9, *B–D*). Local strain was measured with the three principal components of the infinitesimal strain tensor. In all the simulations, the principal basis of strain at the geometric center of the mesh aligned with the global basis of the model, making the infinitesimal strain tensor diagonal. Local strains and volume ratios computed at the geometric center of the FE models were often identical to values calculated using edge displacements. One exception was E_{xx} for the SAC model, which measured a 12.0% compressive strain on edge displacement, but the FE analysis predicted a much smaller compressive strain of 0.9% at the geometric center. This discrepancy was due to the inhomogeneity of E_{xx} along the *x*-axis, with more contraction occurring near the free-edges

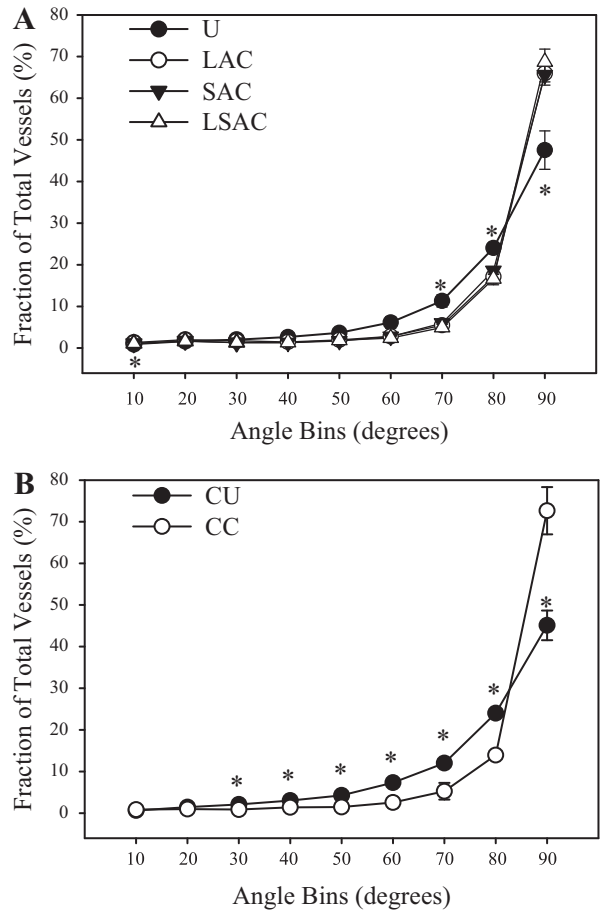

Fig. 7. Microvessel alignment relative to the *z*-axis. Length-normalized distributions of orientation for the hexahedral constructs (*A*) and cylindrical constructs (*B*) are shown. The 10° bin represents angles from 0° to 10°, which are parallel to the *z*-axis of the hexahedral constructs. The 90° bin represents angles from 80° to 90° and is parallel to the XY-plane of the hexahedral constructs. Most of the vessel segments for all of the boundary conditions were parallel to the XY-plane. Significant differences were detected between U and the other groups in the 70°, 80°, and 90° angle bins (*$P < 0.01$). The unconstrained cultures U and CU were significantly different than the other constrained cultures in all but the 10° and 20° angle bins (*$P < 0.05$). Bars indicate standard error.

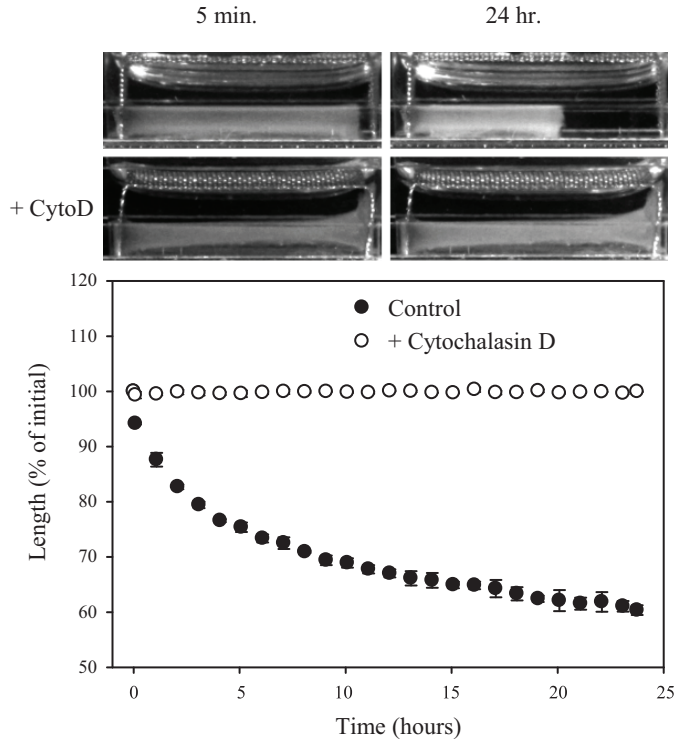

Fig. 8. Contraction of LAC vascularized gels after cutting their attachment to the boundary. To determine whether LAC vascularized gels were under elastic stress due to cell-induced compaction, gel cutting experiments were performed. After 4 days in vitro, LAC gels in the control group were given fresh media, whereas LAC gels in the Cytochalasin D (CytoD) group received fresh media plus 10 μM CytoD. CytoD inhibits actin polymerization. Twenty minutes later, 1 end of the LAC gels was cut free from the boundary constraint using a scalpel. Gels were returned to the incubator, and digital images were captured 5 min later. Imaging continued every 20 min (72 images over 24 h). A glass mirror under the gels was used to obtain multiple culture dimensions. Culture length, height, and width were measured with ImageJ calibrated to optical markers in the same focal plane. *Top*: control LAC gel at 5 min and 24 h after separation from the boundary constraint. *Middle*: LAC gel treated with CytoD at 5 min and 24 h after separation. *Bottom*: remaining length (% of initial length) versus time after cutting. Neither the control nor the CytoD-treated gels exhibited any significant contraction at 5 min after separation. Over the subsequent 24 h, control LAC gels contracted 40% along the long axis. In contrast, the CytoD-treated LAC gels did not exhibit any measureable contraction. These results verify that little if any elastic stress accumulates within the extracellular matrix (ECM) of LAC gels during the culture period, and contraction after separation from the boundary constraint is due to cell contractility.

than at the center of the gel (Fig. 9*A*, *right*). The FE models also predicted that compressive strain along the *z*-axis increased from 35.0% in U boundary conditions to 41.0%, 48.0%, and 48.0% for LAC, SAC, and LSAC cultures, respectively (Fig. 9*D*). This suggests that contraction in the Z-direction increases as boundaries within the XY-plane become more constrained.

Based on the FE strain data above, a correlation between large compressive strains and neovessel alignment was observed, with neovessels oriented perpendicular to the direction of maximum compressive strain. In the center of LAC cultures, large compressive strain along the *y*- and *z*-axes correlated with neovessel alignment along the *x*-axis (Fig. 9). This alignment is solely due to the deformation that the gel experiences during cell-mediated compaction and is independent from any other angiogenic behavior. This was demonstrated by mapping the displacement field at the geometric center of the LAC model to a collection of randomly oriented microvessels. This resulted in a microvessel network that was highly aligned along the long axis, similar to the experimental observations in vitro (Fig. 10). At the geometric center of the SAC cultures, contraction occurred predominantly along the *z*-axis, with very little strain observed along the *x*- and *y*-axis. Consequently, microvessels in these cultures were oriented within the XY-plane. The strain field within the constrained gels was inhomogeneous, and the strain field changed drastically moving from the center toward the edges of the gel. E_{xx} strain was large in the SAC gels between the constraining meshes, but only localized a short distance away from the faces of the gel. Because the compressive E_{zz} strain was also large at this location, we examined the neovessel orientation in the SAC cultures and observed neovessels aligned along the *y*-axis (data not shown). Large E_{yy} and E_{zz} strains were predicted on the outside of the SAC boundaries, where microvessels were oriented parallel to the *x*-axis (data not shown). Circumferential microvessel alignment was observed in the region between the mesh boundary and the edge of the gel in the CC cultures, an area where large compressive radial strain is expected (data not shown).

DISCUSSION

The results of the experiments demonstrated that constraining the boundaries of the 3D vascularized constructs resulted in alignment perpendicular to the direction of maximum compressive strain during angiogenesis. Previously, we observed that neovessels grow and align along the long axis when subjected to static strain loading, cyclic strain loading, or a displacement constraint (24). To better understand how this alignment arises, we examined additional constrained boundary conditions. We found that neovessels were unable to align with respect to the long- or short axis at the geometric centers of the SAC and LSAC cultures, whereas the LAC cultures showed significant alignment parallel to the long axis, as seen previously. From the relative constraints applied by these different conditions, it can be concluded that cell-generated traction forces result in contraction along free edges, producing compressive (negative) strain perpendicular to the free edges. This results in reorientation of collagen fibrils and existing microvessels perpendicular to the contractile direction as cellular traction forces apply result in additional contraction. The logic behind this conclusion is detailed below.

There are at least two possible explanations for neovessel alignment within the LAC constructs: *1*) neovessels align parallel to the direction of greatest tensile stress (1st principal stress) or *2*) neovessels align perpendicular to compressive strain determined by the effective stiffness of the gel. Because the LAC constructs could not change overall length along the *x*-axis, tension could potentially develop along this axis. However, due to the viscoelastic nature of the collagen gels, stresses associated with contraction of vascularized constructs are dissipative rather than cumulative. When LAC constructs were cut free from the boundary constraints, there was no measureable retraction of the constructs over the first 5 min, demonstrating that any stresses that develop within the construct due to cell-generated traction forces had dissipated on a much

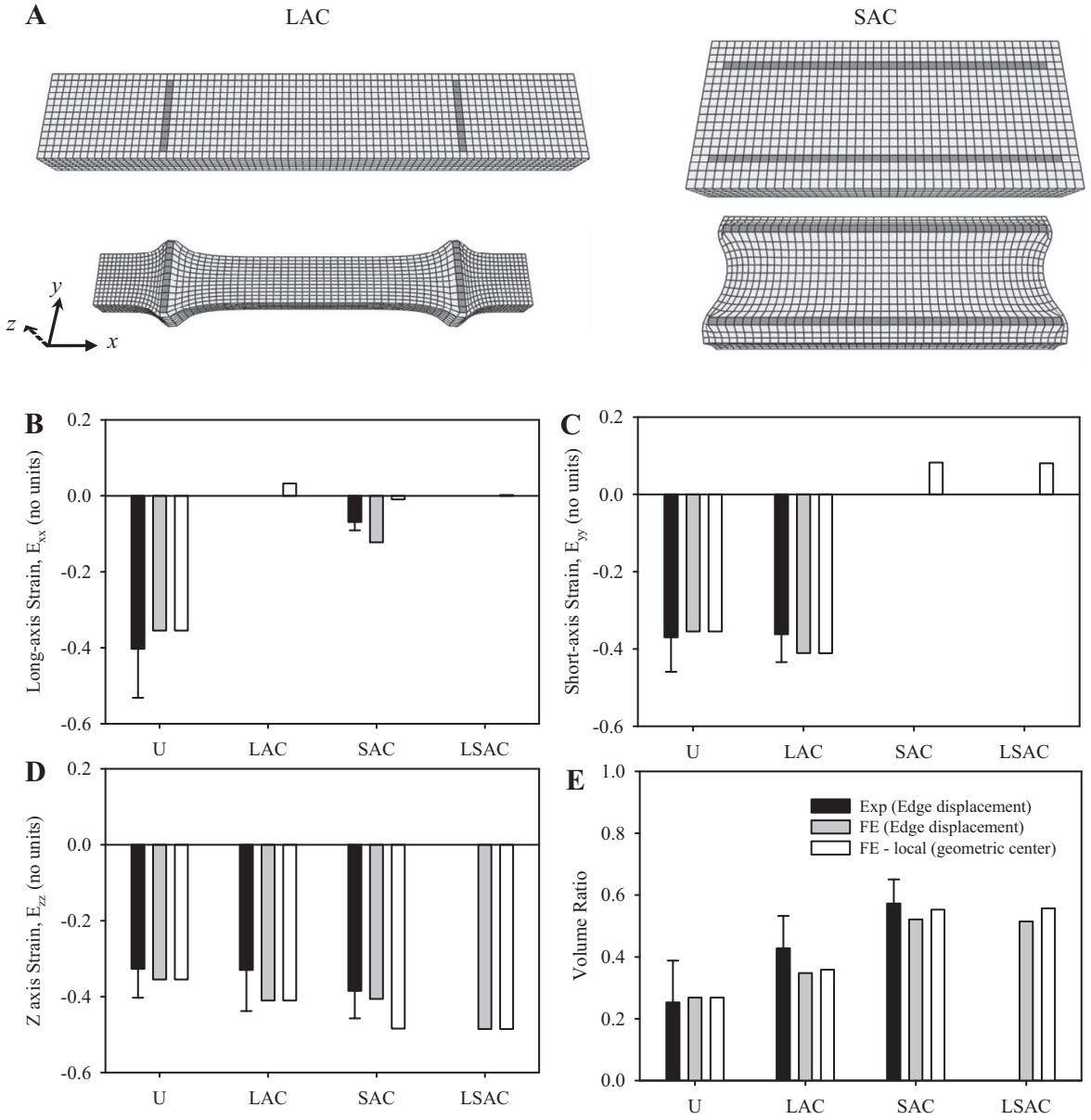

Fig. 9. Finite element (FE) simulations of microvessel-induced contraction of the constrained vascularized constructs. *A*: LAC model is shown at *left*, and the SAC model is shown at *right*. The initial configuration is shown above, and the deformed configuration (i.e., *day 6* of growth) is shown below. *B–E*: global engineering strain was calculated from both the experimental constructs (black) and FE models (gray) using edge displacement and the definition $(L–L_o)/L_o$. Local strain, or the principal components of the infinitesimal strain tensor, was measured for the geometric center of the FE models and reported in white. Engineering strain was calculated along the X-, Y-, and Z-dimension (*B* and *C*), and these results were used to calculate the volume change ratio that occurred over the deformation (*E*). Bars indicate standard error. No bars are present on the FE data (i.e., $N = 1$ simulation).

quicker time scale (Fig. 8). This dissipation occurs over a time scale that is at least three orders of magnitude smaller than the duration of culture (i.e., tens of seconds for stress relaxation versus hundreds of thousands of seconds for the culture duration of 7 days). Cytochalsin D treatment before cutting the gels free from the boundary also prevented gel contraction over the long term, suggesting that cellular traction forces are indeed responsible for culture contraction. Taken together with the observation that neovessels within the SAC cultures were not aligned along the *y*-axis, the direction of 1st principal stress within this boundary condition, this demonstrates that neovessels do not orient along the direction of tensile stress. Tension may indeed arise along the constrained axes of the gels as sprout cells apply contractile forces to the matrix, but this tension is dissipated quickly and before it provides any meaningful directional guidance to growing neovessels.

Coordinately, due to contraction of the ECM, neovessels align along the direction of the greatest effective stiffness secondary to this contraction. There are two sources of stiffness that cells must work against to compact the matrix: stiffness due to the material properties of the matrix and the effective stiffness as influenced by geometric factors. The local effective stiffness is affected by kinematic constraints such as boundary conditions that restrict how the gel can deform during remodeling, and the dimensions of the construct. The effective stiffness is larger along a constrained direction than

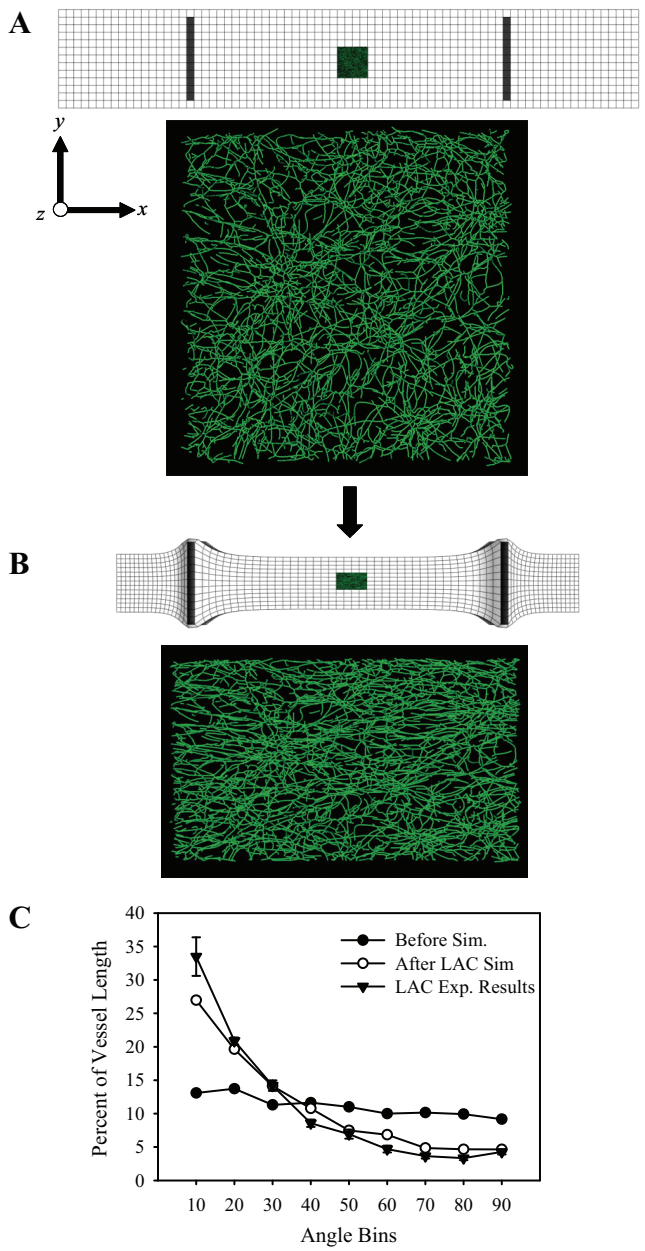

Fig. 10. Anisotropic deformation of the matrix due to cellular contractility is sufficient to cause microvascular alignment, independent of any other cellular behavior. Mapping the displacement field from the LAC FE model onto a distribution of randomly oriented microvessels results in a new alignment pattern that closely resembles alignment within the experimental LAC constructs. *A*: *day 0*, initial mesh geometry with the microvessel dataset positioned at geometric center. *B*: *day 6*, with the use of FE displacement field to map the microvessels, a new alignment pattern emerged due to contraction in the Y- and Z-directions. *C*: length-normalized distributions microvessel angle with the long axis (*x*-axis). The 10° angle bin represents angles from 0° to 10°, which were parallel to the long axis (*x*-axis). The 90° angle bin represents angles from 80° to 90° and was parallel to the short axis (*y*-axis). The angle orientation distribution before mapping (●) indicates random microvessel orientation. After mapping (○), microvessels were preferentially aligned along the long axis. Orientation data from LAC construct experiments are shown as well (▲). Error bars indicate standard error. Sim, simulation.

an unconstrained direction, but the effective stiffness also depends on the geometry of the gel and the boundary conditions. In the LAC cultures, the *x*-axis is constrained but the effective stiffness was low along the *y*- and *z*-axes since the center of the gel was not kinematically constrained by the boundary condition due to the high aspect ratio of the gel. The compressive strain that occurs along the Y- and Z-directions as the gel compacts causes vessels to orient along the relatively stiff *x*-axis as microvessels travel with the compaction of the matrix. In the SAC case, the effective stiffness of the *x*- and *y*-axes is high due to the aspect ratio of the gel and boundary conditions, meaning that the gel only compacted along the *z*-axis. The geometry of the cultures is the primary cause of the increase in effective stiffness when constrained. If the cultures were square and uniaxially constrained, based on these results we would expect microvessels to be aligned along the constrained axis since the effective stiffness along both the vertical and horizontal axes would be the same.

At the geometric center of SAC, LSAC, and CC constructs, E_{xx} and E_{yy} strains were negligible, whereas E_{zz} was negative (compressive). If microvessels align perpendicular to compressive strain, then we would expect vessels to primarily align within the XY-plane for these boundary conditions, which was indeed the case. Compressive strains can also explain the regions of alignment in SAC and CC cultures away from the geometric center. In these regions of the gel, microvessels were aligned perpendicular to the displacement of free edges (data not shown). Therefore, microvessel alignment can be predicted by compressive strain with the gel, with the final deformation field of gel determining vascular topology. Costa et al. (12) studied the effects of similar constrained boundary conditions using human fibroblasts in thin collagen gels. This study showed that fibroblasts were randomly aligned within a fully constrained gel. When one or more of the edges of the gels were unconstrained, the principal axis of individual fibroblasts aligned perpendicular to the dimensions of the gel that were free to contract. The authors concluded that fibroblasts will align parallel to free edges rather than along the direction of greatest tension, but this alignment depends on distance from the free edge (12). Similar studies have demonstrated that anisotropic deformation of the matrix due to cellular compaction results in cellular and matrix fibril alignment (4, 14, 26, 28). These studies involving isolated cells rather than multicellular structures and the results presented in this study demonstrate that anisotropic deformation of the matrix is sufficient to cause alignment in cultures of angiogenic microvessels as well.

Growing neovessels in constrained vascularized constructs that had more constrained boundaries were less branched and, necessarily, exhibited longer segments than those with less constraint. Although there was a significant reduction in apparent vascularity (total length of microvessels/volume) as the number of constrained edges increased (Fig. 5*A*), this morphometric measurement was likely affected by volumetric contraction of the constructs. Because volume ratios were not available for the fully constrained cases (LSAC and CC), we were not able to directly normalize data for these constructs. However, if it is assumed that the volume ratio of the LSAC (or CC) constructs at the geometric center was similar to that of the SAC constructs (0.57), then the amount of volume reduction would be substantially less than what was seen in the U

constructs (0.25). Therefore, fewer units of vessel length per unit of volume will be present within the imaged region of the constrained gels compared with the unconstrained controls. FE models predicted large differences in volume ratios at the geometric center across the hexahedral boundary conditions (Fig. 9): U (0.268), LAC (0.359), SAC (0.535), and LSAC (0.539). It is unclear whether previous studies examining endothelial cell growth accounted for volumetric changes between boundary conditions (39). Regardless, it has been suggested that anchoring matrix boundaries increases the apparent effective stiffness of matrix, thus making it more difficult for cells to contract and remodel the matrix (39). Similar to results for our microvessel constructs, primary endothelial cell cultures exhibit a reduction in growth and morphological parameters as apparent effective stiffness increased, either by higher increasing collagen (matrix) concentrations or by mechanical constraint.

The two other growth parameters measured, average segment length and branching, were not normalized to volume, so matrix contraction did not have a direct impact on these results. However, increased branching in the unconstrained gels may be indirectly caused by matrix contraction. Contraction of the matrix may bring distant neovessels into closer proximity, increasing the probability of these vessels fusing via anastomosis, thereby resulting in more branch points and shorter segment lengths. Computational simulations predict that local chemical factors secreted by endothelial tip cells may increase the likelihood of anastomosis (5).

In all constructs, neovessels primarily grew within the horizontal (XY) plane of the culture (perpendicular to the *z*-axis). Because constructs were imaged to a depth of 300 μm from the surface, it is possible that interactions with the chamber surface during gel polymerization caused vessels to orient within the horizontal plane. Neovessels could also adopt this planar orientation through contact guidance along oriented collagen fibers. Although we were able to image deeper into the constructs (up to 1 mm), the quality of image data at this depth was poor due to light scattering from collagen fibrils, preventing quantitative analysis. Qualitatively, neovessel orientation in unconstrained constructs was random beyond 300 μm from the surface, whereas microvessels in the constrained cultures were still oriented within the XY-plane. These observations correlate well with quantitative results obtain within the first 300 μm of unconstrained cultures, which exhibited less vessel orientation in the XY-plane than the constrained cultures.

The FE analysis demonstrated that the deformation field produced by compaction of the matrix via cellular traction forces in the presence of constrained boundaries is sufficient to explain the global shape changes and alignment results from the experiments. For instance, by applying the displacement field from the FE simulation of a LAC gel to a collection of randomly oriented microvessels, we were able to produce microvessel alignment that closely matched the experimental results (Fig. 10). Furthermore, we were able to match all experimental measurements of global and local strain in the experimental boundary condition groups (LAC, SAC, LSAC) using an active stress parameter p determined from a separate experimental case (U). Nevertheless, there were a number of simplifying assumptions in terms of the material behavior of the constructs, the kinematics of the deformation of the constructs, and the nature of the cellular traction forces. It is possible that nonaffine deformation of microvessels with respect to the matrix and feedback during collagen fibril remodeling may influence the alignment of angiogenic neovessels (42). The vascularized gels were represented by a homogeneous, isotropic nearly linear constitutive model and did not include an explicit representation of microvessels or collagen fibrils. Collagen gels exhibit nonlinear material behavior (38), viscoelasticity (3), and strain induced anisotropy (42). However, the equilibrium material behavior of native collagen gels is nearly linear over a range of tensile strains that do not cause substantial fibril realignment (25). The vascularized constructs are a heterogeneous mixture of acellular collagen and the microvessel population, and both aligned microvessels and collagen fibrils introduce anisotropy (24). These anisotropic effects were not represented in the constitutive model for the passive stress. Additionally, the constitutive model for passive stress represented the equilibrium state of the material and did not include any viscoelastic or biphasic effects. The compaction of the matrix was driven by an active dilatational stress component that was homogeneous and isotropic, neglecting initial or strain-induced anisotropy time-dependent changes in active cellular tractions (3, 4). Collagen gels also exhibit large Poisson's ratio at high uniaxial tensile strains due to reorientation of collagen fibrils during extension, which does not occur under isotropic cell-mediated compaction (43). In our model we assumed a Poisson's ratio of zero, and this assumption would have to be changed if simulations included uniaxial extension. We were unable to find suitable experimental data in the literature to assign the active stress parameter p, so we had to fit this parameter from one of the experimental datasets. Despite these limitations, the FE simulations demonstrated that even the simplest model of gel compaction due to cellular traction forces can describe the results for strain and alignment obtained in all of the experiments (Figs. 9 and 10). This simple model can be extended in the future to include explicit representation of microvessels and the mechanical interaction between sprouts and the ECM, anisotropy, and viscoelastic effects, allowing simulations to reach better fidelity to the vascularized gel experiments and potentially providing further insight into the mechanical regulation of angiogenesis. Additionally, the models could be further validated by measuring local strains in the experimental cultures as a function of growth.

In conclusion, aligned microvascular architecture in vascularized constructs with boundary constraints results from anisotropic strain fields in the ECM produced by cell-generated traction forces. Changing the boundary conditions alters the effective stiffness of the constructs in a mechanically predictable manner, resulting in resistance to contraction by neovessel sprouts, therefore determining the strain field within the construct during growth. These changes in the strain field significantly affected microvessel alignment. In addition, constraining the boundaries of the construct affected the apparent vascularity of collagen gels and the degree of branching and segment length, suggesting that angiogenic growth is promoted by the effective stiffness and the ability of contractile cells to deform the matrix. The results of this study provide a potential explanation for the topology of microvascular networks that arise in tissue in vivo such as skeletal muscle, tendon, and ligament. Additionally, the study provides the basis for using

mechanical boundary conditions to promote and modulate neovascularization of tissue engineered devices (9). The effective stiffness of the matrix can be increased or decreased to either inhibit or promote neovascularization, respectively. Boundary conditions can be manipulated to create anisotropic effective stiffness within the matrix, thus inducing alignment during angiogenesis. Matrices with isotropic stiffness will result in vascular networks with no preferred alignment. These findings also suggest other properties of the matrix that influence effective stiffness, such as matrix density or degree of cross-linking, can also be used to modulate angiogenic growth and to manipulate the orientation of resulting microvascular networks.

GRANTS

Financial support for this study was provided by National Heart, Lung, and Blood Institute Grant R01HL-077683.

DISCLOSURES

No conflicts of interest, financial or otherwise, are declared by the author(s).

AUTHOR CONTRIBUTIONS

Author contributions: C.J.U., J.B.H., and J.A.W. conception and design of research; C.J.U., L.T.E., and J.A.W. performed experiments; C.J.U., L.T.E., and J.A.W. analyzed data; C.J.U., L.T.E., J.B.H., and J.A.W. interpreted results of experiments; C.J.U., L.T.E., and J.A.W. prepared figures; C.J.U., L.T.E., and J.A.W. drafted manuscript; C.J.U., L.T.E., J.B.H., and J.A.W. edited and revised manuscript; C.J.U., L.T.E., J.B.H., and J.A.W. approved final version of manuscript.

REFERENCES

1. **Adams RH, Alitalo K.** Molecular regulation of angiogenesis and lymphangiogenesis. *Nat Rev Mol Cell Biol* 8: 464–478, 2007.
2. **Ateshian GA, Rajan V, Chahine NO, Canal CE, Hung CT.** Modeling the matrix of articular cartilage using a continuous fiber angular distribution predicts many observed phenomena. *J Biomech Eng* 131: 061003, 2009.
3. **Barocas VH, Moon AG, Tranquillo RT.** The fibroblast-populated collagen microsphere assay of cell traction force—Part 2: measurement of the cell traction parameter. *J Biomech Eng* 117: 161–170, 1995.
4. **Barocas VH, Tranquillo RT.** An anisotropic biphasic theory of tissue-equivalent mechanics: the interplay among cell traction, fibrillar network deformation, fibril alignment, and cell contact guidance. *J Biomech Eng* 119: 137–145, 1997.
5. **Bentley K, Mariggi G, Gerhardt H, Bates PA.** Tipping the balance: robustness of tip cell selection, migration and fusion in angiogenesis. *PloS Comput Biol* 5: e1000549, 2009.
6. **Bottenstein JE, Sato GH.** Growth of a rat neuroblastoma cell line in serum-free supplemented medium. *Proc Natl Acad Sci USA* 76: 514–517, 1979.
7. **Carosi JA, Eskin SG, McIntire LV.** Cyclical strain effects on production of vasoactive materials in cultured endothelial cells. *J Cell Physiol* 151: 29–36, 1992.
8. **Chang CC, Krishnan L, Nunes SS, Church KH, Edgar LT, Boland ED, Weiss JA, Williams SK, Hoying JB.** Determinants of microvascular network topologies in implanted neovasculatures. *Arterioscler Thromb Vasc Biol* 32: 5–14, 2012.
9. **Chen X, Aledia AS, Ghajar CM, Griffith CK, Putnam AJ, Hughes CC, George SC.** Prevascularization of a fibrin-based tissue construct accelerates the formation of functional anastomosis with host vasculature. *Tissue Eng Part A* 15: 1363–1371, 2009.
10. **Chien S, Li S, Shyy YJ.** Effects of mechanical forces on signal transduction and gene expression in endothelial cells. *Hypertension* 31: 162–169, 1998.
11. **Clapp C, Thebault S, Jeziorski MC, Martinez De La Escalera G.** Peptide hormone regulation of angiogenesis. *Physiol Rev* 89: 1177–1215, 2009.
12. **Costa KD, Lee EJ, Holmes JW.** Creating alignment and anisotropy in engineered heart tissue: role of boundary conditions in a model three-dimensional culture system. *Tissue Eng* 9: 567–577, 2003.
13. **Deroanne CF, Lapiere CM, Nusgens BV.** In vitro tubulogenesis of endothelial cells by relaxation of the coupling extracellular matrix-cytoskeleton. *Cardiovasc Res* 49: 647–658, 2001.
14. **Fernandez P, Bausch AR.** The compaction of gels by cells: a case of collective mechanical activity. *Integr Biol (Camb)* 1: 252–259, 2009.
15. **Ghajar CM, Chen X, Harris JW, Suresh V, Hughes CC, Jeon NL, Putnam AJ, George SC.** The effect of matrix density on the regulation of 3-D capillary morphogenesis. *Biophys J* 94: 1930–1941, 2008.
16. **Holzapfel GA.** *Nonlinear Solid Mechanics*. John Wiley and Sons, LTD, 2000.
17. **Hoying JB, Boswell CA, Williams SK.** Angiogenic potential of microvessel fragments established in three-dimensional collagen gels. In Vitro *Cell Dev Biol Anim* 32: 409–419, 1996.
18. **Ives CL, Eskin SG, McIntire LV.** Mechanical effects on endothelial cell morphology: in vitro assessment. In Vitro *Cell Dev Biol* 22: 500–507, 1986.
19. **Jalali S, del Pozo MA, Chen K, Miao H, Li Y, Schwartz MA, Shyy JY, Chien S.** Integrin-mediated mechanotransduction requires its dynamic interaction with specific extracellular matrix (ECM) ligands. *Proc Natl Acad Sci USA* 98: 1042–1046, 2001.
20. **James R, Kesturu G, Balian G, Chhabra AB.** Tendon: biology, biomechanics, repair, growth factors, and evolving treatment options. *J Hand Surg Am* 33: 102–112, 2008.
21. **Joung IS, Iwamoto MN, Shiu YT, Quam CT.** Cyclic strain modulates tubulogenesis of endothelial cells in a 3D tissue culture model. *Microvasc Res* 71: 1–11, 2006.
22. **Klagsbrun M, Moses MA.** Molecular angiogenesis. *Chem Biol* 6: R217–R224, 1999.
23. **Krishnan L, Hoying JB, Nguyen H, Song H, Weiss JA.** Interaction of angiogenic microvessels with the extracellular matrix. *Am J Physiol Heart Circ Physiol* 293: H3650–H3658, 2007.
24. **Krishnan L, Underwood CJ, Maas S, Ellis BJ, Kode TC, Hoying JB, Weiss JA.** Effect of mechanical boundary conditions on orientation of angiogenic microvessels. *Cardiovasc Res* 78: 324–332, 2008.
25. **Krishnan L, Weiss JA, Wessman MD, Hoying JB.** Design and application of a test system for viscoelastic characterization of collagen gels. *Tissue Eng* 10: 241–252, 2004.
26. **L′Heureux N, Germain L, Labbe R, Auger FA.** In vitro construction of a human blood vessel from cultured vascular cells: a morphologic study. *J Vasc Surg* 17: 499–509, 1993.
27. **Larrivee B, Freitas C, Suchting S, Brunet I, Eichmann A.** Guidance of vascular development: lessons from the nervous system. *Circ Res* 104: 428–441, 2009.
28. **Lopez Valle CA, Auger FA, Rompre P, Bouvard V, Germain L.** Peripheral anchorage of dermal equivalents. *Br J Dermatol* 127: 365–371, 1992.
29. **Maas S.** *PostVIEW User's Manual, Version 1.4* (Online). Musculoskeletal Research Laboratories, Univ. of Utah, Salt Lake City, UT. http://febio.org/postview/ [23 May 2014].
30. ***Maas WinFiber3D* (Online).** Musculoskeletal Research Laboratories, Univ. of Utah, Salt Lake City, UT. http://mrl.sci.utah.edu/software/winfiber3d [23 May 2014].
31. **Maas SA, Ellis BJ, Ateshian GA, Weiss JA.** FEBio: finite elements for biomechanics. *J Biomech Eng* 134: 011005, 2012.
32. **Matthies H, Strang G.** The solution of nonlinear finite element equations. *Int J Numer Methods Eng* 14: 1613–1626, 1979.
33. **McCormick SM, Frye SR, Eskin SG, Teng CL, Lu CM, Russell CG, Chittur KK, McIntire LV.** Microarray analysis of shear stressed endothelial cells. *Biorheology* 40: 5–11, 2003.
34. **Nunes SS, Krishnan L, Gerard CS, Dale JR, Maddie MA, Benton RL, Hoying JB.** Angiogenic potential of microvessel fragments is independent of the tissue of origin and can be influenced by the cellular composition of the implants. *Microcirculation* 17: 557–567, 2010.
35. **Patrick CW Jr, McIntire LV.** Shear stress and cyclic strain modulation of gene expression in vascular endothelial cells. *Blood Purif* 13: 112–124, 1995.
36. **Pries AR, Secomb TW.** Control of blood vessel structure: insights from theoretical models. *Am J Physiol Heart Circ Physiol* 288: H1010–H1015, 2005.
37. **Rasband WS.** *ImageJ* (Online). U. S. National Institutes of Health. http://imagej.nih.gov/ij/ [23 May 2014].

38. **Reese SP, Ellis BJ, Weiss JA.** Micromechanical model of a surrogate for collagenous soft tissues: development, validation and analysis of mesoscale size effects. *Biomech Model Mechanobiol* 12: 1195–1204, 2013.
39. **Sieminski AL, Hebbel RP, Gooch KJ.** The relative magnitudes of endothelial force generation and matrix stiffness modulate capillary morphogenesis in vitro. *Exp Cell Res* 297: 574–584, 2004.
40. **Sieminski AL, Was AS, Kim G, Gong H, Kamm RD.** The stiffness of three-dimensional ionic self-assembling peptide gels affects the extent of capillary-like network formation. *Cell Biochem Biophys* 49: 73–83, 2007.
41. **Stamatas GN, McIntire LV.** Rapid flow-induced responses in endothelial cells. *Biotechnol Prog* 17: 383–402, 2001.
42. **Thomopoulos S, Fomovsky GM, Chandran PL, Holmes JW.** Collagen fiber alignment does not explain mechanical anisotropy in fibroblast populated collagen gels. *J Biomech Eng* 129: 642–650, 2007.
43. **Vader D, Kabla A, Weitz D, Mahadevan L.** Strain-induced alignment in collagen gels. *PloS one* 4: e5902, 2009.
44. **Vernon RB, Sage EH.** A novel, quantitative model for study of endothelial cell migration and sprout formation within three-dimensional collagen matrices. *Microvasc Res* 57: 118–133, 1999.
45. **Yamamura N, Sudo R, Ikeda M, Tanishita K.** Effects of the mechanical properties of collagen gel on the in vitro formation of microvessel networks by endothelial cells. *Tissue Eng* 13: 1443–1453, 2007.